# Fuel cell electrocatalsis : oxygen reduction on Pt-based nanoparticle catalysts

Vliet, D.F. van der

# Chapter 6

## Platinum-alloy Nanostructured Thin Film Catalysts for the Oxygen Reduction Reaction

In an effort to increase fuel cell activity for the oxygen reduction reaction (ORR), a range of metallic alloy nanostructured thin film (NSTF) catalysts have been manufactured by 3M and measured both at room temperature and at 333K. Characterization of the particles was done ex-situ by microscopy and X-Ray diffraction and in situ by the rotating disk electrode (RDE). Optimal loadings for the ORR were established and activities superior to carbon supported nanoparticles (Pt/C) have been recorded. The most active catalyst was a 55 weight%$_{Pt}$ PtNi alloy, which is an order of magnitude more active than Pt/C in kinetic current, and an improvement factor of 2.5 in mass activity. Lowering the platinum content of this catalyst did not lead to increased mass activity values.

## 6.1 Introduction

The need for clean cars as well as a more efficient use of energy rather than burning fuel in internal combustion engines instigated many companies to make fuel cell operated devices and vehicles available to the general public [1]. A major challenge lies in optimizing the oxygen reduction reaction (ORR) in the fuel cell [2-5], especially to make fuel cells operable in large-scale automotive applications. This challenge sparked a concentrated effort to improve fuel cell catalysts [2, 3, 6-16] to meet the department of energy (DOE) targets [17].

One of the busiest fields currently is the development of high surface area catalysts. These catalysts are usually carbon-supported, which is accompanied by many problems, such as contact problems, particle dissolution [18-20] and agglomeration [19, 21] and carbon support corrosion [19, 22, 23]. It has been shown that the nanostructured thin film (NSTF) catalysts of 3M [21, 24, 25], which has no carbon support, are much more stable in a membrane electrode assembly (MEA) than any supported nanoparticulate catalyst [17].

For this reason the activity for the ORR of a range of PtNi and PtCo based multimetallic NSTF catalysts has been measured, both at room temperature and at 333K - a temperature close to the more ideal operating temperature (353K [5]) of a current polymer electrolyte fuel cell (PEFC). At temperatures higher than 333K, the water evaporation of the electrolyte would be too severe to measure the catalysts properly in the rotating disk electrode (RDE) setup. The proper loadings for the NSTF in RDE testing were established in detail, and activites are reported for the NSTFs measured with the appropriate loading.

The most active catalyst found in this work is the PtNi binary NSTF catalyst with mass activities exceeding those of carbon supported high surface area catalysts. The PtCo-based catalysts were significantly less active than their nickel-containing counterparts. A PtNiCo ternary catalyst was also tested, the activity of which resembles the other PtCo catalysts closely and does not approach the level of the PtNi and PtNiFe catalysts. Finally, the content of Pt in the alloy was reduced in an effort to lower total Pt loading of the catalyst. Unfortunately, this did not lead to increased kinetic activities, and hence also did not yield increased mass activities.

## 6.2 Experimental

The metallic NSTF catalyst was manufactured by 3M as reported previously [24, 25]. In brief, the desired metals were sputtered consecutively on a perylene red film. This creates the so-called nanostructured thin film (NSTF) catalyst. In order to facilitate measurements in RDE, the individual whiskers were brushed off the manufactured films and stored as a powder. The Pt/C catalyst used in this work is a state-of-the-art 5 nanometer sized Pt catalyst from Tanaka (TKK, Tokyo), supported on vulcan.

To prepare the suspension needed for electrode preparation for the thin film RDE method [26], a small glass bottle was cleaned in a beaker with acid and boiled repeatedly with Milli-Q $H_2O$ (18.2 MΩ resistivity, less than 4 ppb toc). About 2 mg of NSTF catalyst powder was weighed into the bottle and 2 ml Milli-Q water added. Next, the suspension was sonicated for at least 30 minutes before use. A pre-polished Glassy Carbon (GC) disc of 6 mm in diameter was mounted in a KLF leak-free collet. The collet with GC disc inserted was cleaned in concentrated perchloric acid for 10 minutes, followed by extensive rinsing with Milli-Q water. Prior to the experiment the resistance of the disc in the collet was checked to assure the absence of electrical resistance. The GC disk in the collet is then polished with 0.05 μm aluminum oxide, followed by rinsing with Milli-Q $H_2O$ and cleaning in acid. A measured volume of the sonicated catalyst suspension, was then pipetted onto the GC disc. The collet was put onto a hotplate at 40°C in an Ar atmosphere and left to dry. After the electrode had dried, the surface was rinsed with Milli-Q water to wash off the loosely bonded particles and subsequently protect the surface from contamination and exposure to atmospheric gases. The electrolyte was in all cases 0.1M $HClO_4$, prepared by diluting concentrated 70% concentrated perchloric acid (Grade ACS, AMD Chemicals). The electrolyte was made in batches of 500 ml; stored in a teflon flask which was cleaned beforehand in a mixture of concentrated nitric and sulfuric acid, and rinsed extensively with Milli-Q water.

A standard in-house 3-electrode cell was used in all measurements. An Ag / AgCl electrode in equilibrium with the electrolyte separated from the cell by a salt bridge was used as the reference electrode. The Luggin-Haber capillary was positioned as close to the cell as possible without disturbing the flow by rotation of the electrode, generally at about 10 mm distance from the surface of the disk. Any residual Ohmic losses were compensated for by positive feedback in the potentiostat. The reference electrode was calibrated daily with a reversible hydrogen electrode (RHE) in the

electrolyte used that day. All potentials reported here are reported with respect to the RHE. The counter electrode was a Pt mesh. The potentiostat used was an Autolab PGSTAT 30 with ECD, scan-gen and FI-20 modules, in combination with the Autolab GPES software.
The glass electrochemical cell was of in-house design, with a heating jacket built into the cell for measurements at elevated temperatures.

## 6.3 Results and Discussion

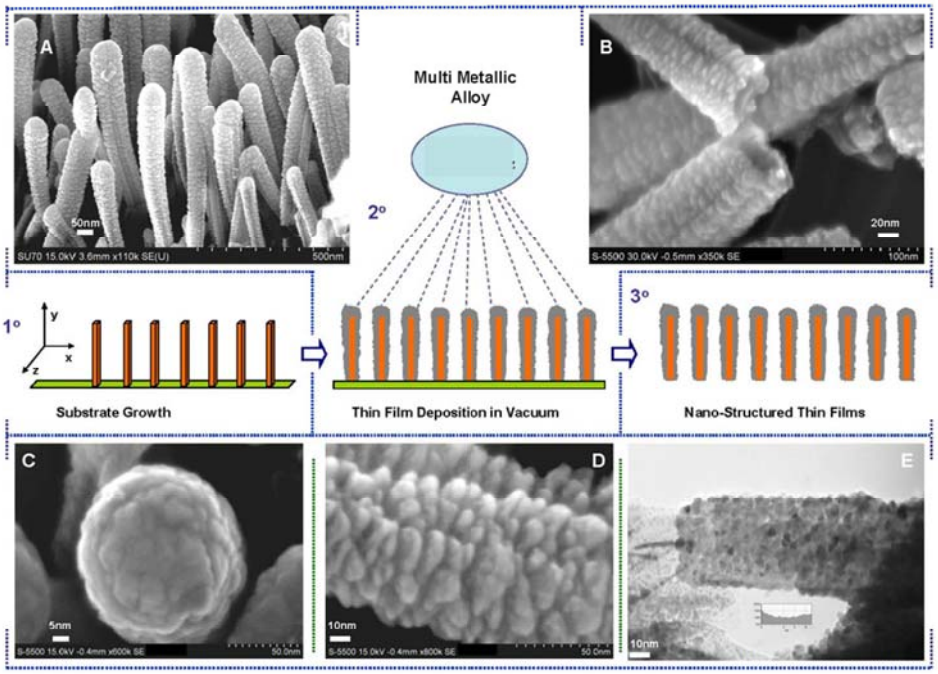


**Figure 6.1, TEM (E) and SEM images (A-D) of 3M NSTF catalysts with schematic representation of deposition in the middle.**

### 6.3.1 Microscopy

TEM and SEM images of the catalysts as received from 3M Company are shown in figure 6.1. The figure shows clearly the unique structure of the catalyst which resembles long rods, studded with rough atomic stumps. Images of this catalyst have been published before in [21, 27]. The middle part of figure 6.1 shows a

graphic representation of the deposition process. Consecutive layers of platinum and the respective metal in the alloy were sputtered on a crystallized organic pigment (*N*,*N*-di(3,5-xylyl)perylene-3,4:9,10bis(dicarboximide), in short: perylene red) in Ultra High Vacuum (UHV) [24, 25]. The sputtering covered each of the perylene reds whiskers with a thin metallic film. Platinum and nickel were sputtered in sequence on the substrate, resulting in a metal-covered, whiskered polymer, shown in the electron microscope images in figure 6.1. For our experiments we deposited this catalyst on the GC disk in the RDE setup by first brushing the individual whiskers off the supporting polymer and then suspending them in a small bottle with milli-Q water. The resulting suspension was pipetted on the disk and left to dry in argon, with the amount of suspension pipetted determining the loading of Pt on the disk.

### 6.3.2 Determination of proper platinum loading

Before activity measurements could be commenced, the proper loading of particles on the glassy carbon needed to be determined. Mayrhofer et al [28] determined this to be 42 $\mu g_{pt}\ cm^{-2}_{disk}$, while 3M company uses a loading of 0.1 $mg_{Pt}\ cm^{-2}$ on their fuel cell cathode [21]. Our determination of the optimal loading is shown in figure 6.2. Part A of the figure shows the full oxygen reduction reaction (ORR) curves in 0.1 M perchloric acid with a rotation of 1600 rpm. The curves compare well to those reported before [27, 28]. The influence of the loading is illustrated in this graph:

First, the potential at half the diffusion limiting current, the so-called half-wave potential ($E_{1/2}$) increases linearly with loading from 42 to 130 $cm^{-2}_{disk}$, shown in detail in figure 6.2B. The increasing value for $E_{1/2}$ with increasing loading makes the traditional measure of activity (overpotential at half-wave) difficult to apply for this catalyst, unless the loading is kept constant. Also, high loading decreases the potential window of the kinetic region (at currents lower than half the diffusion limiting current) and can introduce larger errors from reading the current at the steep part of the slope [26].

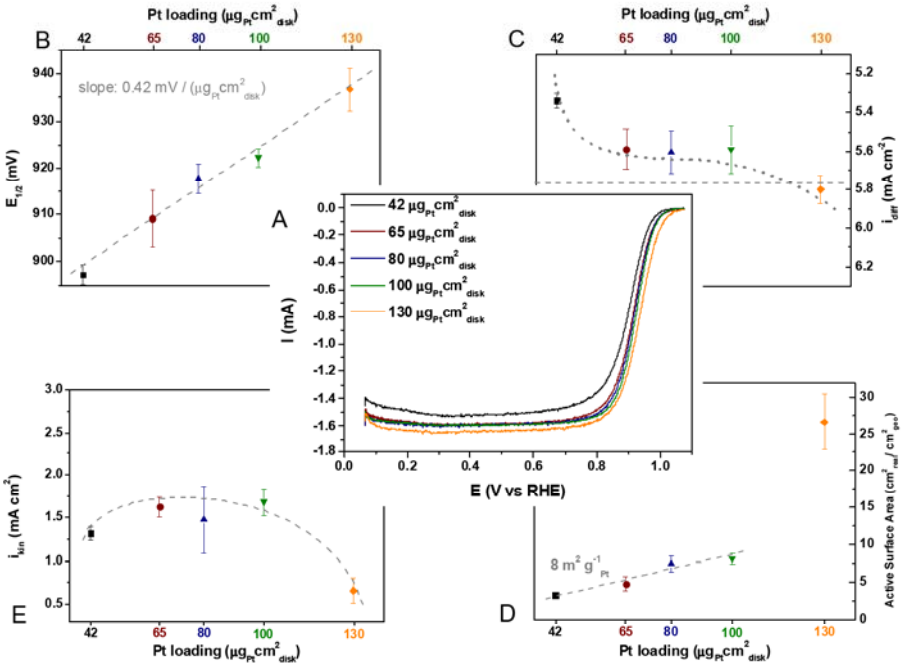


**Figure 6.2, effect of loading of the NSTF catalyst on glassy carbon. A shows the full ORR curves, measured at 293K with a rotation of 1600 rpm and a scan rate of 20 mV $s^{-1}$ in 0.1 M $HClO_4$. Shown in the surrounding graphs is the effect of the loading on half-wave potential (B), diffusion limiting current for the ORR (C), active surface area as measured from $H_{upd}$ (D) and kinetic current density for the ORR at 0.9V vs RHE (E). Standard deviations of a minimum of 3 measurements are given in error bars.**

Secondly, the diffusion limiting current ($I_{diff}$) increases with increasing loading, with a stable region from 60 to 100 $\mu g_{Pt}$ $cm^{-2}_{disk}$, as shown in figure 6.2C. This is in agreement with experiments of Mayrhofer *et al.*, who claim measurements with lower diffusion limiting currents still exhibit the same kinetic current densities when properly corrected for the diffusion contribution [28], but a proper diffusion limiting current is recommended. The diffusion limiting current observed in the experiment is also a measure of distribution. Even at higher loadings $I_{diff}$ will occasionally be lower than theoretically expected. This is indicative of a poor catalyst distribution on the GC disk, with part of the glassy carbon area uncovered by the NSTF and thus exposed, and other spots on the disk too thickly coated. When the loading is increased above 100 $cm^{-2}_{disk}$, $I_{diff}$ increases again, this is because the catalyst layer becomes thicker than the diffusion layer and the accepted mass-transport characteristics for the RDE are not satisfied anymore [29, 30].

Furthermore, the active surface area (SA) increases (of course) with increasing loading. As can be seen in figure 6.2D, this is a linear trend until about 100 $\mu g_{Pt}$ $cm^{-2}_{disk}$, with a surface area of about 8 $m^2$ per gram of Pt. This is 20% lower than the value of 10 $m^2$ $g^{-1}$ reported before [21] in an actual MEA. The effect of the support (GC) cannot be ruled out in this respect, and the shielding of part of the surface of the NSTF by the glassy carbon can result in a lower active surface area per gram of Pt. Interestingly, at higher loadings the SA increases more than linearly. This coincides with the appearance of the higher diffusion limiting current as mentioned before, and is indicative of a multi-layer of catalyst particles on the disk. The surface area at high loading is puzzling as it exceeds the value reported for the MEA, we found the approximate surface area per mass for high loadings to be around 20 $m^2$ $g_{Pt}^{-1}$, double the value reported for the same catalyst in a MEA [21]. This effect has to our knowledge not been observed before and further investigation would be required to find the origin.

Finally what this means for the activity, *i.e.* the kinetic current at 0.9V versus RHE, is shown in figure 6.2E. Clearly, lower and higher loadings have a reduced activity for the ORR. At low loadings, the SA is harder to determine, which causes the lower apparent activity. In other measurements on the alloys (not shown in figure 6.2), lower loadings actually gave increased activity values due to the under-estimation of the active surface area by $H_{upd}$ charge. It is best to avoid these troubles and remain slightly higher in loading, though not as high as 130 $\mu g_{Pt}$ $cm^{-2}_{disk}$, where the more than linearly increased surface area suppressed the kinetic current.

After taking these observations into consideration we determined the ideal loading in these experiments to be 65 $\mu g_{Pt}$ $cm^{-2}_{disk}$; low enough to avoid problems due to the increased activity and to not waste Pt (and thus to keep mass activities relatively high), yet high enough to avoid problems with distribution and surface area determination. All further figures and data reported here are measured with 65 $\mu g_{Pt}$ $cm^{-2}_{disk}$.

### 6.3.3 Blank Cyclic Voltammetry

Different alloy and monometallic Pt catalysts were considered in this research. Three bimetallic catalysts: $Pt_3Co$, $Pt_3Ni$ and $PtNi_2$ and four trimetallic catalysts; a $Pt_{0.32}Ni_{0.61}Fe_{0.07}$ alloy, a $Pt_{0.67}Co_{0.30}Mn_{0.03}$ alloy, a $Pt_{0.4}Co_{0.5}Zr_{0.1}$ alloy, and a $Pt_3CoNi$ alloy.

For the ease of comparison of the cyclic voltammograms (CVs) the catalysts will be divided into two categories; one group containing platinum nickel alloys (PtNi of

various compositions and PtNiFe ternary alloy) and the other group containing Pt cobalt alloys (PtCo, PtCoMn and PtCoZr). There was also a PtCoNi ternary alloy, which falls into both categories, and of course there is monometallic Pt NSTF.

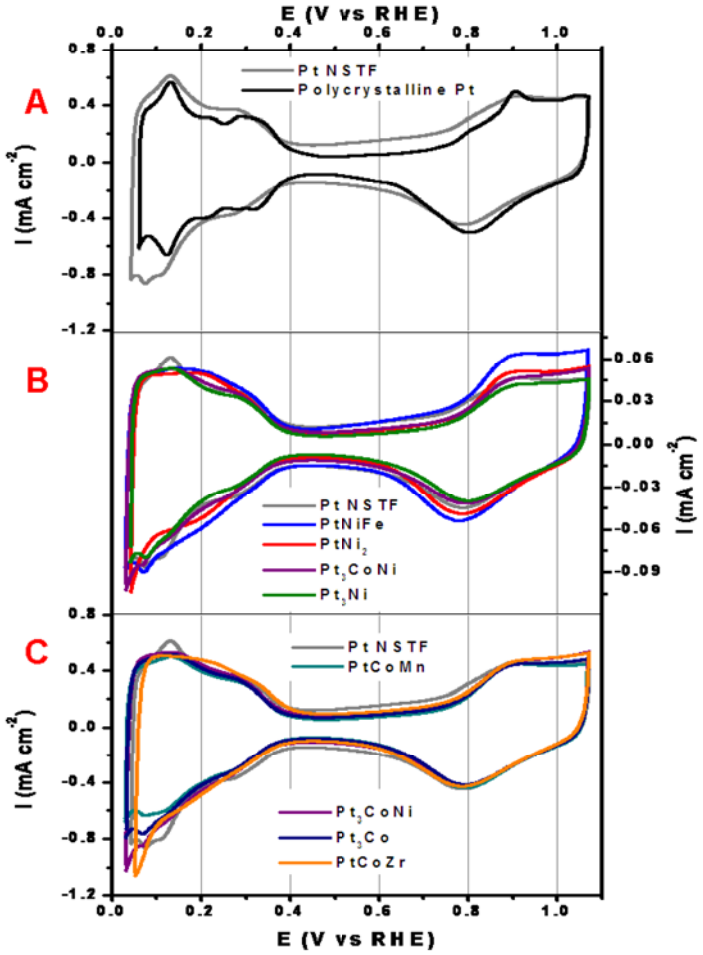


**Figure 6.3. Blank cyclic voltammetry for the various NSTF catalysts. All were measured at 293K in 0.1M $HClO_4$ with 50 mV $s^{-1}$. Part A shows the comparison between monometallic Pt NSTF and polycrystalline bulk platinum. The various Nickel and Cobalt-based catalysts are shown in B and C respectively. The loading of the NSTF catalyst was 65 $\mu g_{Pt}$ $cm^{-2}_{disk}$.**

Blank CVs are shown in figure 6.3, with the Ni samples in part B and the Co samples in part C. To make a good comparison between nanostructured catalysts and extended surfaces, a comparison with bulk polycrystalline Pt is in order (figure 6.3A). The underpotentially deposited hydrogen ($H_{upd}$) region at potentials lower

than 0.4V exhibits much broader features for the NSTF catalyst. This is a first indication that on the thin film catalyst a plethora of lower coordinated Pt atoms are on the surface and the crystalline islands are smaller than on poly Pt. This is confirmed by the higher affinity for surface oxide, with the oxide reduction peak shifted about 25 mV lower for the NSTF catalyst. The magnitude of adsorption of oxides (as determined from the charge of oxide formation in figure 6.3A) on Pt NSTF is higher immediately positive of the onset of surface oxide formation at 0.75V, see figure 6.4A. This charge offers a convenient way to compare adsorption on the catalysts without the influence of the double layer charging, which is much higher for the NSTF catalyst due to the glassy carbon support.

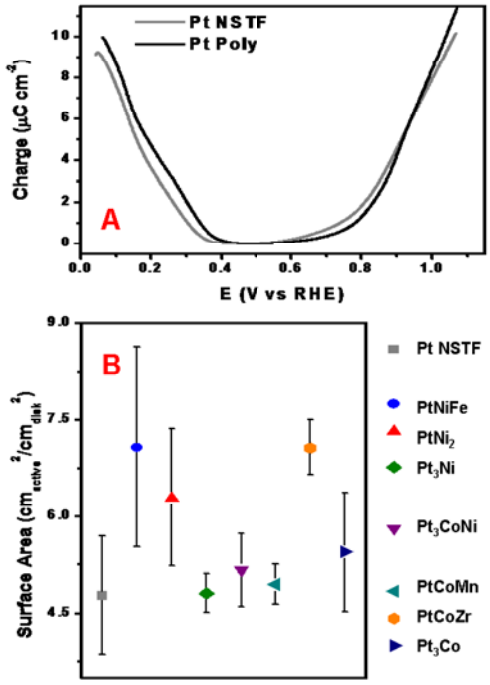


**Figure 6.4. Part A shows the comparison in adsorption isotherm between monometallic Pt NSTF and polycrystalline bulk platinum; this is the charge under the blank CV after double-layer correction. The surface areas of the various Nickel and Cobalt-based catalysts are shown in part B, compared to the Pt NSTF as well. The loading of the NSTF catalyst was 65 $\mu g_{Pt}$ $cm^{-2}_{disk}$.**

It is clear that the differences in cyclic voltammetry between the alloy catalysts are subtle. PtNiFe and $PtNi_2$ show a different $H_{upd}$ region. The maximum in that region is reached at a higher potential than in case of the monometallic NSTF. $Pt_3Ni$ and PtCoNi exhibit similar CVs, both closely resembling the blank CV of Pt NSTF. The

double layer of the alloy electrodes is very dependent on the polishing of the GC substrate and can differ from experiment to experiment as the disk is rougher. Also, the capacity of the double layer is independent of the active surface area of the catalyst and as the figure is normalized for this active surface area, the double layer capacity seems largest on the catalysts with lower active SA. There is even less difference between the various cobalt containing catalysts, where only PtCoZr exhibits the broader $H_{upd}$ region seen with PtNiFe and $PtNi_2$ as well. From figure 6.4B it is concluded that these three catalysts have the largest surface area of the catalyst per gram Pt at a loading of 65 $\mu g_{Pt}$ $cm^{-2}_{disk}$. The alloys are expected to have a higher specific surface area, as the non-noble elements from the alloy dissolve upon contact with the electrolyte [31], thereby roughening the surface. Moreover, becausese the surface of monometallic Pt NSTF is already rough (see the electron microscope images in figure 6.1), the increase would be expected to be minimal. As is evident from figure 6.4, this expectation holds true for most catalysts, but PtNiFe, $PtNi_2$ and PtCoZr catalysts have an increased surface area compared to the other catalysts due to their reduced Pt content in the compositions relative to the other alloys, with 32, 33 and 40 atomic-% respectively. This increased surface area also explains the broader $H_{upd}$ features mentioned before, as there is less crystallinity and a larger amount of low-coordinated Pt surface atoms.

### 6.3.4 Oxygen Reduction Reaction

The results for the oxygen reduction reaction (ORR) are shown in figure 6.5. The loading of the NSTF catalysts was 65 $\mu g_{Pt}$ $cm^{-2}_{disk}$. Tafel plots are shown in part A-C to graphically compare the activity for the NSTF catalysts over a range of 0.85 to 0.95V. It can be seen that there is not a definite linear relation between log of the current versus the potential (Tafel slope). It is clear that the monometallic Pt NSTF catalyst offers a large improvement versus carbon supported Pt catalyst, see figure 6.5A. The Pt/C used in our work has a loading of 17 $\mu g_{Pt}$ $cm^{-2}_{disk}$; a higher loading will lead to diffusion layer problems. This catalyst is itself three times more active than the commercial Pt/C catalysts [32]. Therefore, the Pt NSTF catalyst has an improvement of close to an order of magnitude versus the reported Pt/C, as claimed before [28]. Obvious from figure 6.5B is the high activity for the ORR for the low-Pt content PtNi-catalysts, PtNiFe and $PtNi_{2.5}$, an order of magnitude versus the 5 nm TKK catalyst, and 3 times more active than the monometallic Pt NSTF. The other nickel-containing and the cobalt-based catalysts are very similar in activity, as can be seen in figure 6.5C. The catalytic specific activity is better illustrated in

figure 6.6, in which the half-wave potential (A) and kinetic current at 900 mV versus RHE (B) are compared. Again, the obvious conclusion from this graph is that the two catalysts with high nickel content; *i.e.* PtNiFe and $PtNi_2$ are superior in activity to the other NSTFs and completely overshadow the Pt/C catalyst.

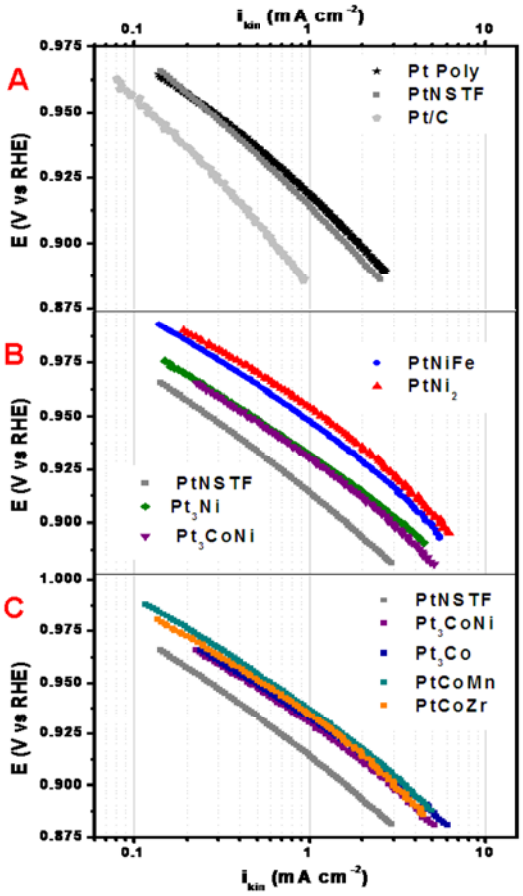


**Figure 6.5. ORR on NSTF catalysts, compared to polycrystalline Pt. Tafel plots are shown in A for the monometallic Pt sample, compared to Pt poly and state of the art Pt/C catalyst, and B and C show the Ni and Co based alloys respectively.**

This is true even when we consider the mass activities at 900 mV versus RHE, shown in figure 6.6C. Carbon supported nanoparticles usually have high mass activities, because one of the main advantages of these nanoparticles is the high surface area to mass ratio. This high ratio means that there is a lot of active surface area per gram of platinum, for example about 50 $m^2$ platinum surface area per gram

of Pt for a carbon-supported 5 nm sized catalyst, as determined from our reference experiments. This is a factor of 5 higher than the typical value for the NSTF catalysts. However, from our experiments we can conclude that the PtNi alloy NSTF catalysts actually have a higher mass activity than the carbon supported Pt nanoparticles in addition to higher kinetic activities.

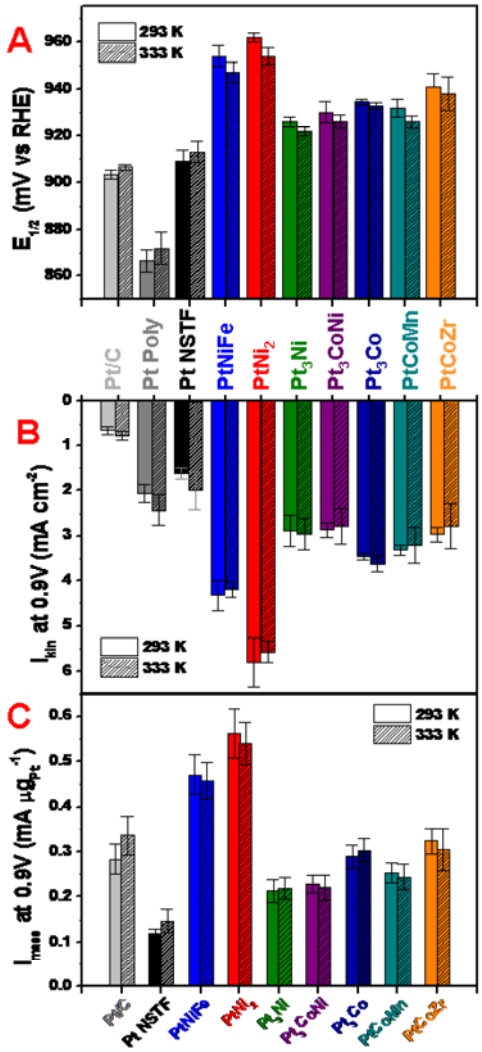


**Figure 6.6. Bar graphs of the ORR on NSTF catalysts, compared to polycrystalline Pt. Part A shows the half-wave potential ($E_{1/2}$) for loadings of 65 $\mu g_{Pt}$ $cm^{-2}_{disk}$ for the NSTF catalysts and 18 $\mu g_{Pt}$ $cm^{-2}_{disk}$ for the Pt/C and the kinetic and mass current densities at 0.9V are shown in part B and C, respectively. The single-color bars represent the value at 293 K, and the accented bars represent 333 K.**

Finally, the Pt content in the PtNi alloy was lowered in an effort to increase mass activity even further. Figure 6.7 shows the results for the ORR activity at 0.9 V vs RHE, both in kinetic and in mass activity. The blank cyclic voltammetries of these catalysts (not shown) are essentially identical. It is clear that the kinetic currents decrease when the platinum content is lowered, but the expected increase in mass activity due to increased Pt surface area being available, is not observed. Based on the catalysts measured, the PtNi alloy with about 55 wt-% platinum is the best catalyst.

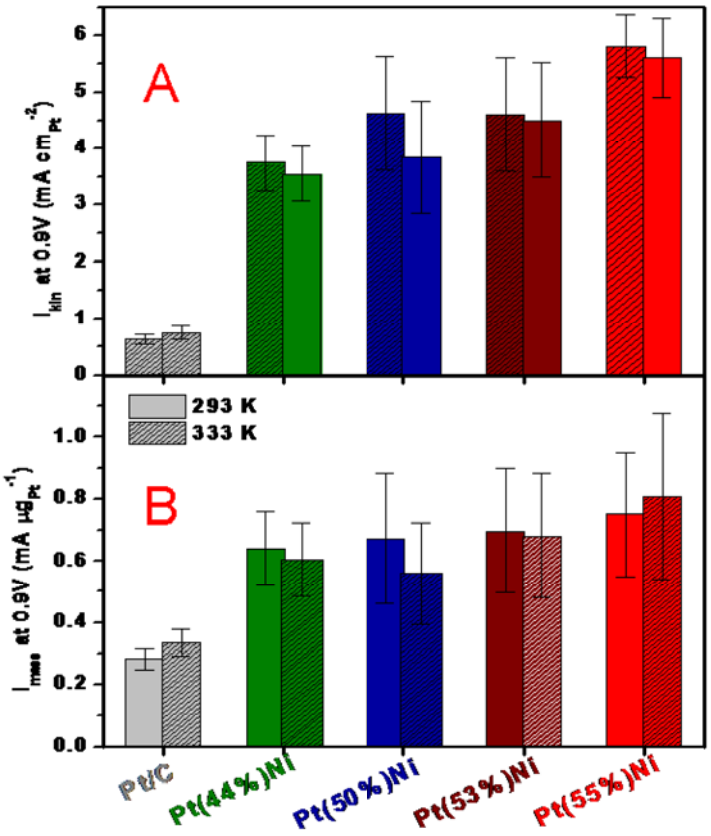


**Figure 6.7. Bar graphs of the ORR on PtNi catalysts with different Pt content. Light grey bars show the Pt/C catalyst as a reference. The kinetic and mass current densities at 0.9V are shown in part A and B, respectively. Loadings of 65 $\mu g_{Pt}$ $cm^{-2}_{disk}$ for the NSTF catalysts and 18 $\mu g_{Pt}$ $cm^{-2}_{disk}$ for the Pt/C were used. The single-color bars represent the value at 293 K, and the accented bars represent 333 K.**

## 6.4 Conclusion

A range of multimetallic platinum-based nanostructured thin film catalysts, manufactured by 3M, have been measured in the rotating disk electrode setup. These nanoparticles are not dispersed on vulcan, but directly deposited on glassy carbon; in the actual membrane electrode assembly, they are non-carbon supported. The surface of these particles is shown to be very rough, full of low-coordinated platinum.

The optimal loading for RDE measurements in our setup was determined to be 65 $\mu g_{Pt}\ cm^{-2}_{disk}$; a higher loading will give rise to problems with the diffusion layer, and anomalous behavior of the surface area per gram of particles, while a lower loading will leave parts of the glassy carbon disk uncovered, and cause the diffusion limiting current to be lower than the expected value for a 6 mm disk electrode.

Of all catalysts measured, the PtNi alloys show more promising activities for the ORR than the PtCo based alloys. Especially the PtNi, and PtNiFe alloys are very active. Furthermore, these alloys have a higher active surface area per gram of platinum, which means that their mass activities are superior to any of the other catalysts measured. The mass activities of PtNi and PtNiFe even exceed those of 5 nm platinum nanoparticles on vulcan.

Finally, the Pt content in the PtNi alloy was lowered in an effort to increase mass activity even further, but it was found that when the Pt content is lowered below 55 mass%, this does not lead to an increased mass activity.

So far, the most active catalyst measured, both in kinetic current and in mass activity, is the PtNi alloy with 55 mass% platinum. Further experiments will be necessary to optimize the platinum content in the alloy. Furthermore, the layer thickness of the sputtered layer on the perylene red may be reduced, which will increase the Pt utilization and give increased mass activity values. It is clear from our experiments, that the NSTF catalyst is a very promising ORR catalyst, with increased activities compared to any other nanoparticulate catalyst currently available.

## References

[1] B. Johnston, M. C. Mayo, and A. Khare, Technovation. 25 (2005) 569.

[2] H. A. Gasteiger, S. S. Kocha, B. Sompalli, and F. T. Wagner, Applied Catalysis B-Environmental. 56 (2005) 9.

[3] H. A. Gasteiger, J. E. Panels, and S. G. Yan, Journal of Power Sources. 127 (2004) 162.
[4] M. C. Tucker, Journal of Power Sources. 195 (2010) 4570–4582.
[5] H. A. Gasteiger and M. F. Mathias, in: M. Murthy, T. F. Fuller, J. W. Van Zee, and S. Gottesfeld, (Eds), Proton conducting membrane fuel cells III: proceedings of The Electrochemical Society, Vol. 2002-31, The Electrochemical Society, Inc., Pennington, New Jersey, 2005, p. 1.
[6] K. J. J. Mayrhofer, B. B. Blizanac, M. Arenz, V. R. Stamenkovic, P. N. Ross, and N. M. Markovic, Journal of Physical Chemistry B. 109 (2005) 14433.
[7] J. X. Wang, N. M. Markovic, and R. R. Adzic, Journal of Physical Chemistry B. 108 (2004) 4127.
[8] L. Xiao, L. Zhuang, Y. Liu, J. T. Lu, and H. D. Abruna, Journal of the American Chemical Society. 131 (2009) 602.
[9] J. Hernandez, J. Solla-Gullon, E. Herrero, A. Aldaz, and J. M. Feliu, Journal of Physical Chemistry C. 111 (2007) 14078.
[10] L. G. R. A. Santos, K. S. Freitas, and E. A. Ticianelli, Electrochimica Acta. 54 (2009) 5246.
[11] A. S. Arico, P. Bruce, B. Scrosati, J. M. Tarascon, and W. Van Schalkwijk, Nature Materials. 4 (2005) 366.
[12] A. Atkinson, S. Barnett, R. J. Gorte, J. T. S. Irvine, A. J. Mcevoy, M. Mogensen, S. C. Singhal, and J. Vohs, Nature Materials. 3 (2004) 17.
[13] P. Strasser, S. Koh, T. Anniyev, J. Greeley, K. More, C. Yu, Z. Liu, S. Kaya, D. Nordlund, H. Ogasawar, M. F. Toney, and A. Nilsson, Nature Chemistry. Published online: 25 April 2010 | doi:10.1038/nchem.623 (2010).
[14] K. J. J. Mayrhofer and M. Arenz, Nature Chemistry. 1 (2009) 518.
[15] J. Greeley, I. E. L. Stephens, A. S. Bondarenko, T. P. Johansson, H. A. Hansen, T. F. Jaramillo, J. Rossmeisl, I. Chorkendorff, and J. K. Norskov, Nature Chemistry. 1 (2009) 552.
[16] D. Strmcnik, K. Kodama, D. van der Vliet, J. Greeley, V. R. Stamenkovic, and N. M. Markovic, Nature Chemistry. 1 (2009) 466.
[17] K. E. Martin, J. P. Kopasz, and M. K.W., Fuel Cell Chemistry and Operation, Chapter 1, 2010, p. 1.
[18] K. Kinoshita, J. Lundquist, and P. Stonehart, Journal of Electroanalytical Chemistry. 48 (1973) 157.
[19] S. S. Zhang, X. Z. Yuan, J. N. C. Hin, H. J. Wang, K. A. Friedrich, and M. Schulze, Journal of Power Sources. 194 (2009) 588.
[20] K. J. J. Mayrhofer, S. J. Ashton, J. C. Meier, G. K. H. Wiberg, M. Hanzlik, and M. Arenz, Journal of Power Sources. 185 (2008) 734.
[21] M. K. Debe, A. K. Schmoeckel, G. D. Vernstrorn, and R. Atanasoski, Journal of Power Sources. 161 (2006) 1002.
[22] V. Komanicky, K. C. Chang, A. Menzel, N. M. Markovic, H. You, X. Wang, and D. Myers, Journal of the Electrochemical Society. 153 (2006) B446.
[23] Y. Y. Shao, J. Wang, R. Kou, M. Engelhard, J. Liu, Y. Wang, and Y. H. Lin, Electrochimica Acta. 54 (2009) 3109.
[24] M. K. Debe and A. R. Drube, Journal of Vacuum Science & Technology B. 13 (1995) 1236.
[25] M. K. Debe and R. J. Poirier, Journal of Vacuum Science & Technology a-Vacuum Surfaces and Films. 12 (1994) 2017.

[26] T. J. Schmidt, H. A. Gasteiger, G. D. Stab, P. M. Urban, D. M. Kolb, and R. J. Behm, Journal of the Electrochemical Society. 145 (1998) 2354.
[27] A. Bonakdarpour, K. Stevens, G. D. Vernstrom, R. Atanasoski, A. K. Schmoeckel, M. K. Debe, and J. R. Dahn, Electrochimica Acta. 53 (2007) 688.
[28] K. J. J. Mayrhofer, D. Strmcnik, B. B. Blizanac, V. Stamenkovic, M. Arenz, and N. M. Markovic, Electrochimica Acta. 53 (2008) 3181.
[29] F. Gloaguen, P. Convert, S. Gamburzev, O. A. Velev, and S. Srinivasan, Electrochimica Acta. 43 (1998) 3767.
[30] J. Perez, E. R. Gonzalez, and E. A. Ticianelli, Electrochimica Acta. 44 (1998) 1329.
[31] V. R. Stamenkovic, B. S. Mun, K. J. J. Mayrhofer, P. N. Ross, and N. M. Markovic, Journal of the American Chemical Society. 128 (2006) 8813.
[32] P. J. Ferreira, G. J. la O', Y. Shao-Horn, D. Morgan, R. Makharia, S. Kocha, and H. A. Gasteiger, Journal of the Electrochemical Society. 152 (2005) A2256.